

LETTER

# High-Sn fraction GeSn quantum dots for Si-based light source at 1.55 $\mu\text{m}$

To cite this article: Lu Zhang *et al* 2019 *Appl. Phys. Express* **12** 055504

View the [article online](#) for updates and enhancements.

## Recent citations

- [GeSn/SiO<sub>2</sub> Multilayers by Magnetron Sputtering Deposition for Short-Wave Infrared Photonics](#)  
Adrian Slav *et al*
- [Effects of Annealing on the Behavior of Sn in GeSn Alloy and GeSn-Based Photodetectors](#)  
Liming Wang *et al*
- [Epitaxial GeSn obtained by high power impulse magnetron sputtering and the heterojunction with embedded GeSn nanocrystals for SWIR detection](#)  
Ioana Dascalescu *et al*



## High-Sn fraction GeSn quantum dots for Si-based light source at 1.55 $\mu\text{m}$

Lu Zhang<sup>1</sup>, Haiyang Hong<sup>1</sup>, Cheng Li<sup>1\*</sup>, Songyan Chen<sup>1</sup>, Wei Huang<sup>1</sup>, Jianyuan Wang<sup>1</sup>, and Hao Wang<sup>2</sup>

<sup>1</sup>Semiconductor Photonics Research Center, OSED, Department of Physics, Jiujiang research institute, Xiamen University, Xiamen, Fujian 361005, People's Republic of China

<sup>2</sup>Research Institute for Soft Matter and Biomimetics, Department of Physics, Xiamen University, Xiamen, Fujian 361005, People's Republic of China

\*E-mail: lich@xmu.edu.cn

Received January 30, 2019; revised February 20, 2019; accepted February 22, 2019; published online April 9, 2019

The preparation of GeSn quantum dots (QDs) facilitates the solution of Si-based light source for communication. The GeSn QDs with a uniform size of 5 nm embedded in amorphous GeSn were synthesized by low temperature annealing on amorphous GeSn strips intersected with Sn strips. The Sn fraction in GeSn QDs is much higher than that in original amorphous GeSn matrix. A novel growth mechanism related to Sn diffusion induced nucleation and the strain limitation effect was proposed. The direct bandgap of  $\sim 0.8$  eV extracted from room-temperature photoluminescence and absorption spectra is larger than the theoretical prediction of 0.41 eV in bulk GeSn with Sn fraction of 13.6%.

© 2019 The Japan Society of Applied Physics

**G**e<sub>1-x</sub>Sn<sub>x</sub> alloy with Sn fraction larger than about 0.1 is revealed to achieve the transition from indirect to direct bandgap<sup>1,2)</sup> and higher carrier mobility as compared with Ge.<sup>3,4)</sup> Consequently, it has been a candidate for the next generation of Si-compatible electronic and photonic devices.<sup>5)</sup> However, the low solid solubility of  $\alpha$ -Sn in Ge below 1 atom% and large lattice mismatch between  $\alpha$ -Sn and Ge hinder the development of high-Sn fraction GeSn.<sup>6,7)</sup> In addition, the energy bandgap (0.3–0.5 eV) of the direct bandgap GeSn alloy is narrower compared to the optical communication wavelength ( $\sim 0.8$  eV), limiting its potential in near-infrared (NIR) optoelectronics. To solve the above issues, reducing the size of crystalline GeSn into nanoscale is one of the most possible paths. GeSn QDs,<sup>8–10)</sup> nanowires,<sup>11,12)</sup> and quantum wells<sup>13,14)</sup> have been demonstrated enhancing the optical efficiency for applications in Si-based electronic and photonic devices. GeSn QDs with the maximum surface to volume ratio among them, provide more opportunities for dislocations to relax during the doping of Sn atoms and the bandgap can be modulated by the quantum confinement effect as the size less than the Bohr exciton radius (24.3 nm for Ge).<sup>15,16)</sup>

To date, multiple approaches have been proposed for GeSn nanocrystals synthesis, such as Sn-rich GeSn nanocrystals in a Ge matrix using molecular beam epitaxy,<sup>8)</sup> colloidal GeSn nanocrystals based chemical methods,<sup>10,17,18)</sup> GeSn nanocrystals using a gas-phase laser photolysis reaction,<sup>19)</sup> and so on. However, the methods above could not simultaneously satisfy the following requirements: (1) uniform size and Sn fraction with high density ( $>10^{10}$  cm<sup>-2</sup>); (2) emitting at optical communication wavelengths of approximately 1310 or 1550 nm; (3) emitting at room temperature; and (4) integration of Si with the complementary metal oxide semiconductor (CMOS)-compatible fabrication technique. Therefore, more efficient and cost-effective methods are still needed.

In this work, we report the fabrication of high-Sn GeSn QDs with average size of 5 nm based on Sn diffusion using a low-cost co-sputtering technique. In virtue of low preparation temperature, high-Sn GeSn QDs without  $\beta$ -Sn segregation or defects have been demonstrated. The highly dense GeSn QDs of  $6 \times 10^{11}$  cm<sup>-2</sup> and the achievement of room-temperature photoluminescence (RT PL) spectra at  $\sim 1.55$   $\mu\text{m}$  are very promising for optoelectronic device applications.

The amorphous GeSn (a-GeSn) film of 45 nm thickness were grown on Si substrates covered with 800 nm SiO<sub>2</sub> films by magnetron co-sputtering techniques at room temperature. The sputtering pressure was kept 0.5 Pa in argon ambient. The Sn fraction of a-GeSn was 2% controlled by adjusting sputtering power. Amorphous Ge films were also deposited as well for comparison. After that, amorphous GeSn and Ge films were patterned into narrow strips (width: 3.6  $\mu\text{m}$ , length: 150  $\mu\text{m}$ ) using lift-off process. Subsequently, 50-nm-thick Sn strips with 1.2  $\mu\text{m}$  width using lift-off process were deposited perpendicular to the amorphous GeSn and Ge strips, respectively, with 25  $\mu\text{m}$  away from one end. Finally, after capping with 500-nm-thick SiO<sub>2</sub> layers, the samples were heat-treated in a tubular annealing furnace at low temperature of 300 °C in nitrogen atmosphere from 0.5 to 40 h. The samples of unannealed a-GeSn film (annotated as reference sample) and annealed GeSn strips without Sn strip on them (annotated as contrast sample) were also prepared for comparison.

The Sn fraction, crystalline characterization, morphology and size of GeSn nanocrystals were characterized by high resolution transmission electron microscopy (HRTEM) and Raman spectroscopy (wavelength: 532 nm). The Sn diffusion process along the GeSn strips were demonstrated with the energy dispersive spectrometer (EDS). The energy band parameters of GeSn nanocrystals were studied by absorption and PL spectra with excitation laser at wavelength of 532 nm and power of 10 mW at room-temperature.

As the cross-section TEM image shown in Fig. 1(a), GeSn nanocrystals of sample annealed at 300 °C for 40 h is represented as the black dots with average size of 5 nm and cross-section density of  $6 \times 10^{11}$  cm<sup>-2</sup>. The structure and cross-section of the sample are schematically shown in Fig. 1(b). As the HRTEM image shown in Fig. 1(c), clear lattice fringes without  $\beta$ -Sn aggregation in the GeSn nanocrystal indicate high crystallinity. Figure 1(d) depicts the fast Fourier transform (FFT) pattern taken from the same place as in Fig. 1(c). Bright spot marked with dark arrow exhibits highly (220) textured GeSn nanocrystal and the Sn fraction is calculated to be about 13.6%, which is much larger than the Sn fraction in the initial a-Ge<sub>0.98</sub>Sn<sub>0.02</sub>.

As shown in Fig. 2(a), the Raman peak from Ge–Ge mode of sample annealed for 40 h is asymmetric of the left and right. The shoulder on the left of the Ge–Ge mode peak is

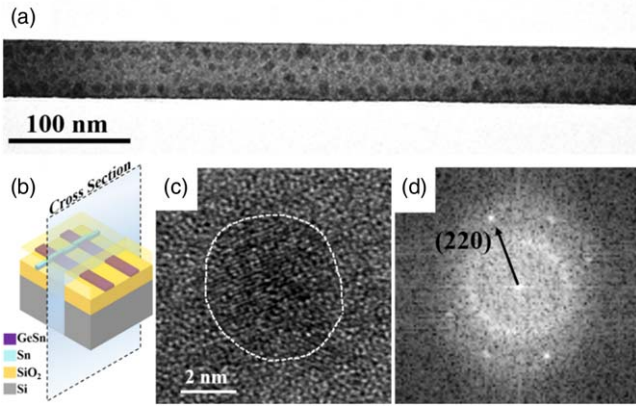


**Fig. 1.** (Color online) (a) Cross-section TEM image of the sample annealed at 300 °C for 40 h. (b) The sketch of the sample. (c) HRTEM image of the GeSn nanocrystal. (d) FFT pattern taken from the same place as in (c).

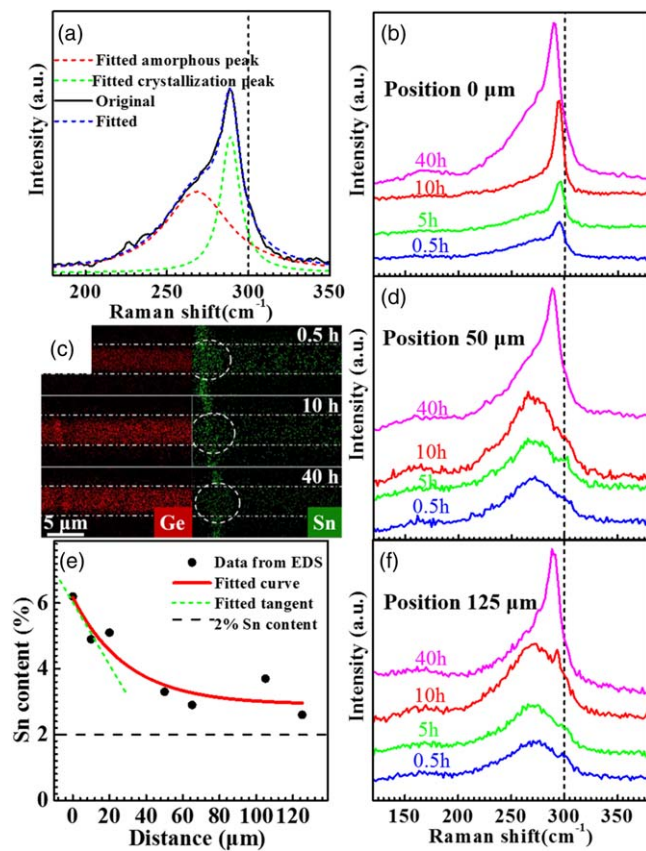


**Fig. 2.** (Color online) (a) Raman spectra of sample annealed at 300 °C for 40 h. The black line, as well as the blue, green and red dotted lines represent the original, fitted data, the crystalline and amorphous peaks, respectively. Raman spectra of samples annealed at different timings from 0.5 to 40 h at positions of 0 (b) 50 (d) and 125 μm (f) away from the Sn strip edge, respectively. (c) Ge and Sn EDS element mappings of samples after annealing for 0.5, 10 and 40 h, respectively. (e) Sn fraction distribution along GeSn strip from 0 to 125 μm after annealing for 40 h.

attributed to the disorder in the bond distances of a-GeSn. The green and red dotted Lorentzian curves by fitting indicate the crystalline and amorphous peaks, respectively. The crystallinity, namely the  $\text{Ge}_{1-x}\text{Sn}_x$  nanocrystals ratio in a-GeSn matrix can be expressed as:

$$\eta = \frac{A_c}{A_c + A_a} \quad (1)$$

where  $A_c$  and  $A_a$  are defined as the areas of the crystalline and amorphous peaks, respectively. The calculation yields  $\eta$  of 32.6%, which demonstrates a high proportion of  $\text{Ge}_{1-x}\text{Sn}_x$  nanocrystals in a-GeSn matrix. The crystalline peak shift  $\Delta\omega$  compared to Ge–Ge Raman peak from bulk Ge (black dotted line) can be attributed to Sn substitution of Ge into the lattice. As a result, Sn fraction  $x$  is 13.7% calculated by  $\Delta\omega = -82x$ ,<sup>20</sup> which is broadly in line with the data from HRTEM.

To investigate the formation mechanism of GeSn nanocrystals in detail, crystallinity at different positions in GeSn strips after heat treatment from 0.5 to 40 h were characterized one by one. Figure 2(b) shows Raman spectra measured at the Sn strip edge intersected with GeSn strip (position 0 μm). Here, a-GeSn annealed at 300 °C for 0.5 h began to crystallize with the Sn fraction of 7.1%. The crystalline peak intensity manifests to be proportional to annealing time and the Sn fraction increased to 13.7% for 40 h. At positions of 50 and 125 μm away from the Sn strip edge, the crystalline peaks appear as the annealing time prolong to 40 h, as shown in Figs. 2(d) and 2(f).

As the EDS element mappings shown in Fig. 2(c), the obvious Sn diffusion along GeSn strips from the intersection (white dotted circle) is observed with the increase of annealing time. Obviously, the red curve fitted for Sn fraction distribution of sample with 40 h annealing confirms the diffusion of Sn from intersection end to the other, as shown in Fig. 2(e). And by making the tangent of this curve, a maximum absolute value at 0 μm is extracted as 0.095% μm<sup>-1</sup>, which means negligible Sn fraction difference among positions in the GeSn strip.

As shown in Fig. 3(a), both the contrast and reference samples keep the original amorphous phase without any GeSn crystalline peak. This further validates the importance of the Sn diffusion for the formation of GeSn nanocrystals. Besides, the same amorphous characteristic of both the contrast and reference samples faultlessly precludes the stress induced crystallization caused by the encapsulated SiO<sub>2</sub>. The crystallinity of the sample with pure Ge strips intersected with Sn strip differs from the sample of GeSn strip. As shown in Figs. 3(b) and 3(c), after being treated at 300 °C for 40 h, pure Ge strip appears similarly partly crystallization at 0 and 50 μm away from Sn strip as the GeSn strip sample does. However, Raman peak positions of crystalline Ge–Ge mode in the former shift to higher energy, indicating lower Sn fraction (2.9%–7.2%) in the crystalline GeSn as compared to the latter. Strikingly, no crystalline peak at 125 μm in the Ge strip sample is obtained. According to Ge and Sn EDS element mappings in Fig. 3(d), an obvious Sn diffusion along the Ge strip is revealed while at position 10 μm, the Sn element becomes unapparent. Besides, higher maximum Sn gradient of 18.37% μm<sup>-1</sup> and less diffusion at the same positions can be observed on the inset as compared to Fig. 2(e). This illustrates that the accomplishment of Sn diffusion in a-GeSn needs much longer time than in a-GeSn, which possesses more vacancies due to addition of Sn. Consequently, Sn contained in a-GeSn strip is appreciated to the diffusion of Sn and the formation of high-Sn GeSn crystalline. Nevertheless, it immoderately increases the initial

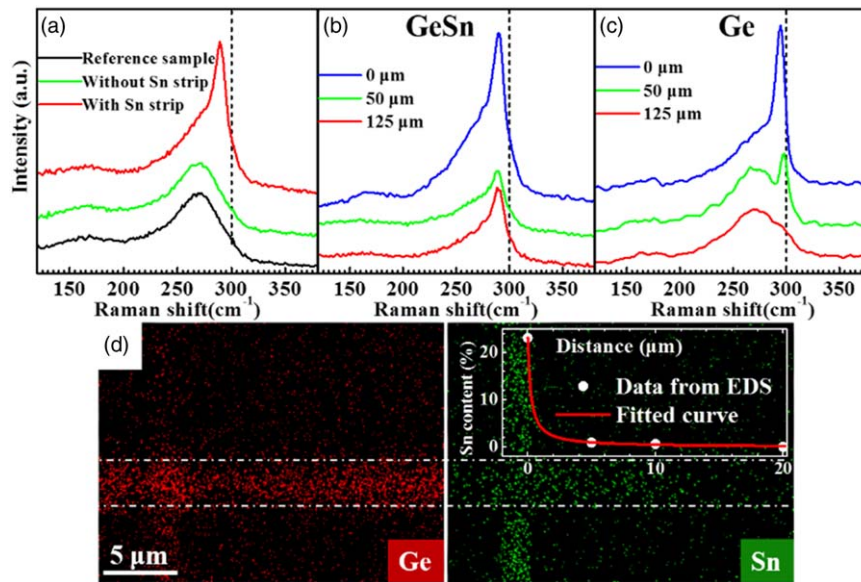


**Fig. 3.** (Color online) (a) Raman spectra of samples with (red line) and without (green line) Sn strip, and reference sample (black line) without annealing. Raman spectra of samples of GeSn (b) and Ge (c) strips both with Sn strips after annealing at 300 °C for 40 h. The blue, green and red lines represent Raman spectra measured at the position 0, 50 and 125  $\mu\text{m}$  away from the Sn strip, respectively. (d) The Ge and Sn EDS element mappings for Ge strip sample annealed at 300 °C for 40 h. The Sn density distribution along Ge strip from 0 to 20  $\mu\text{m}$  is presented on the inset.

Sn fraction in a-GeSn strip would inevitably decrease the nucleation temperature, leading to polycrystalline GeSn.<sup>21,22)</sup>

Based on the above results, the process of GeSn nanocrystals formation can be analyzed by thermodynamics and kinetics in details. The change in Gibbs free energy  $\Delta G$  of nucleation is defined as a sum of two terms: (1) the chemical potentials difference  $\Delta\mu$  of  $N$  molecules (atoms, ions) between the mother  $\mu_{\text{mother}}$  and the new phase  $\mu_{\text{new}}$ , and (2) the free energy penalty  $\Phi$  imposed due to the formation of the new interface,<sup>23)</sup>

$$\Delta G = -N\Delta\mu + \Phi \quad (2)$$

where  $-N\Delta\mu = N(\mu_{\text{new}} - \mu_{\text{mother}})$  is negative because the new phase is more stable than the old one. At the start of nucleation, the surface energy  $\Phi$  plays a major role and decreases with increase of Sn atoms due to the weaker bond of Ge-Sn. As a result, the barrier and critical size of nucleation decrease with more Sn atoms, as shown in Fig. 4(c). At 300 °C, the thermal energy  $k_B T$  (blue dash line) is too small to meet the requirement for crossing the energy barrier of  $\text{Ge}_{0.98}\text{Sn}_{0.02}$  nucleation (red solid line). Incorporation of more Sn atoms by diffusion reduces the energy barrier, and the nucleation, which is schematically shown in Figs. 4(a) and 4(b), begins when the barrier is as low as the thermal energy.

For monomers, growth of crystals larger than critical size is persistent without considering the constituent. However, the crystallization of GeSn alloy is more complicated since the component changes depending on conditions. As aforementioned, lower surface energy leads to lower energy barrier for crystallization. Considering the crystal nucleus grows as a consequence of the crystallization of adjacent shell a-GeSn layer, as depicted in Fig. 4(d), there is a tendency that more Sn atoms are favored for the newly crystallized surface. Thanks to the fact that the diffusion coefficient of Sn atom in Ge ( $\sim 10^{-6} \text{ nm}^2 \text{ s}^{-1}$ )<sup>24)</sup> is much larger than that of a Ge atom ( $\sim 10^{-8} \text{ nm}^2 \text{ s}^{-1}$ ),<sup>25)</sup> Sn atoms

move faster than Ge atoms, resulting in local nonuniformity of Sn concentration in a-GeSn. Once the Sn atoms move into the adjacent shell layer, where the Sn atom energetically favorable, a higher Sn fraction GeSn crystalline layer formed. Consequently, more Sn atoms in the amorphous diffuse to the nanocrystal surface and the crystal continues to grow larger no matter Sn concentration of ambient a-GeSn is low or high. As shown in Fig. 2(b), the Raman peaks of Ge-Ge mode from crystallized GeSn shifts to lower energy side as annealing time increases, indicating more Sn incorporated in the nanocrystals. Nevertheless, as the Sn fraction increases shell by shell, more compressive strain, which improves the crystallization energy barrier, is introduced simultaneously at the surface. Therefore, thermal energy becomes insufficient again for overcoming the energy barrier, and the nanocrystals stop growing. As a result, a saturated size of  $\sim 5$  nm GeSn nanocrystals with saturated high Sn fraction of  $\sim 13\%$  were achieved by Sn diffusion induced as well as the strain limited growth mechanism.<sup>26)</sup> This also explains the contradiction in the formation of high quality single crystalline GeSn alloy with high Sn fraction and evokes the promising future of high-Sn fraction with high crystallinity GeSn nanocrystals.

The absorption coefficient of GeSn nanocrystals sample was extracted by transmittance spectra, as shown in Fig. 5(a). We observed the direct absorption edge between 0.76 and 0.82 eV as well as disorder-induced Urbach absorption tail below the bandgap. Near the direct band edge, the interband absorption could be expressed as<sup>27)</sup>

$$(\alpha\hbar\nu)^2 = A(\hbar\nu - E_g^\Gamma) \quad (3)$$

where  $\alpha$  is the absorption coefficient of direct bandgap transition,  $\hbar\nu$  is the photon energy,  $A$  is the constant and  $E_g^\Gamma$  is the direct bandgap energy. By fitting the absorption coefficient of band edge, the direct bandgap energy  $E_g^\Gamma$  of 0.77 eV was extracted, as shown in Fig. 5(b). The direct bandgap  $E_{\text{bulk}}$  of bulk  $\text{Ge}_{0.864}\text{Sn}_{0.136}$  is about 0.41 eV calculated by<sup>28)</sup>

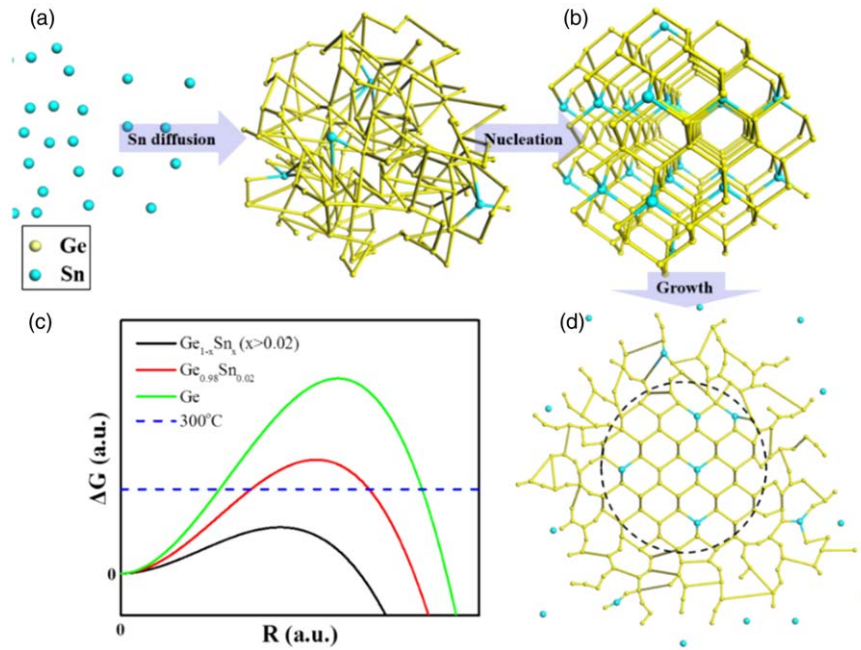


Fig. 4. (Color online) Schematic illustration of (a), (b), (d) the GeSn nanocrystals formation and (c) the change in Gibbs free energy  $\Delta G$ , versus nucleation radius  $R$ .

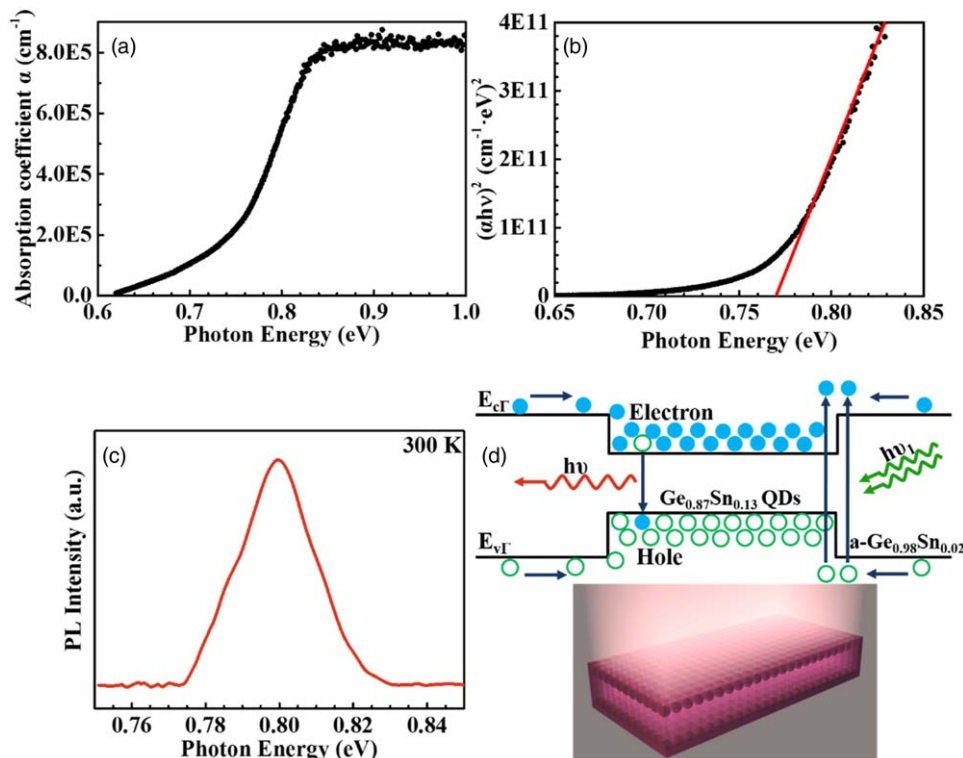


Fig. 5. (Color online) (a) The absorption coefficient of GeSn nanocrystals sample. (b) The data fitting of absorption edge for direct bandgap energy. (c) RT PL spectrum of GeSn QDs sample. (d) Schematic illustration of energy band diagram and photoluminescence.

$$E_{\text{bulk}} = (1 - x)E_g^\Gamma(\text{Ge}) + xE_g^\Gamma(\text{Sn}) - bx(1 - x) \quad (4)$$

where  $E_g^\Gamma(\text{Ge}) = 0.8 \text{ eV}$  and  $E_g^\Gamma(\text{Sn}) = -0.41 \text{ eV}$  are the direct bandgaps of Ge and Sn, respectively. We use the bowing parameter  $b = 1.94 \text{ eV}$ .<sup>29)</sup>

The significant difference between  $E_g^\Gamma$  extracted from the absorption coefficient and the calculated values can be attributed to the energy separation induced by quantum

confinement effect. The absorption energy of nanocrystals with size less than the Bohr exciton radius  $a_B^*$  can be calculated by the theoretical formula<sup>30,31)</sup>

$$E = E_{\text{bulk}} + \frac{\hbar^2\pi^2}{2\mu R^2} - 1.786\frac{e^2}{\epsilon R} - 0.248\frac{e^2}{8\pi\epsilon a_B^*}. \quad (5)$$

Here,  $R$  is the size of the nanocrystal,  $\hbar$  is Planck's constant,  $\epsilon$  is the dielectric constant of the concerned material,  $e$  is the electron charge, and  $\mu = (m_e^{-1} + m_h^{-1})^{-1}$  is the reduced

mass of carriers given by the effective mass of electrons and holes. For  $\text{Ge}_{0.9}\text{Sn}_{0.1}$  alloy, the effective mass of electrons and holes are 0.05 and 0.3  $m_0$  (static electron mass).<sup>32)</sup> Therefore, the absorption energy is 0.75 eV calculated by Eqs. (4), (5).

Furthermore, the RT PL was carried out to directly examine the bandgap and actual luminescence of the nanocrystals. As shown in Fig. 5(c), the PL peak located at  $\sim 0.8$  eV, which fell in the range of optical communication wavelengths ( $\sim 1.55$   $\mu\text{m}$ ), is attributed to the direct radiative recombination occurring in the GeSn nanocrystals. Moreover, the narrow half width at half maximum  $\Delta_{HWHM} = 0.02$  eV of the PL peak demonstrates the uniform size of GeSn nanocrystals. Theoretically calculated bandgap of  $\text{Ge}_{0.864}\text{Sn}_{0.136}$  nanocrystals with size of 5 nm is about 0.75 eV, which is in good agreement with both the experimental results of absorption and RT PL spectra whereas deviating largely from the theoretical bandgap 0.41 eV of  $\text{Ge}_{0.864}\text{Sn}_{0.136}$  bulk. As a result, the  $\text{Ge}_{0.864}\text{Sn}_{0.136}$  nanocrystals are demonstrated to be QDs. As illustrated in Fig. 5(d), the narrower bandgap of  $\text{Ge}_{0.864}\text{Sn}_{0.136}$  QDs compared with that of a- $\text{Ge}_{0.98}\text{Sn}_{0.02}$  is conducive to enhance the luminescence due to the trapping of electrons and holes in the QDs. Therefore, the demonstrated high-Sn GeSn QDs embedded in a-GeSn matrix is promising for the integrate photonic device applications.

In summary, direct bandgap high-Sn fraction GeSn QDs with average size of 5 nm embedded in a-GeSn matrix with high density ( $6 \times 10^{11} \text{ cm}^{-2}$ ) induced by Sn diffusion have been prepared. The high crystallinity of  $\text{Ge}_{0.864}\text{Sn}_{0.136}$  QDs without  $\beta$ -Sn aggregation has been demonstrated. With the assistance of initial Sn in a-GeSn strips, the Sn strip intersected with a-GeSn strips serves as the main diffusion source of Sn for the high-Sn fraction GeSn QDs formation during the annealing. We attribute saturated size and Sn fraction of the GeSn QDs to the strain limited growth mechanism. The direct bandgap energy of GeSn QDs has been extracted as 0.8 eV, which is larger than the bandgap of 0.41 eV in bulk GeSn alloy with the same Sn fraction due to the quantum confinement effect. The RT PL at 1.55  $\mu\text{m}$  (0.8 eV), which fell in the range of optical communication wavelengths, consolidates the achievement of direct band high-Sn fraction GeSn QDs and its potential to applications of near infrared optoelectronics.

**Acknowledgments** This work is supported by the National Natural Science Foundation of China (61474094), National Basic Research Program of China (2013CB632103) and the Fundamental Research Funds for the Central Universities (20720170019).

- 1) C. Eckhardt, K. Hummer, and G. Kresse, *Phys. Rev. B - Condens. Matter Mater. Phys.* **89**, 1 (2014).
- 2) J. Zheng, S. Wang, Z. Liu, H. Cong, C. Xue, C. Li, Y. Zuo, B. Cheng, and Q. Wang, *Appl. Phys. Lett.* **108**, 2 (2016).

- 3) J. Zheng, Z. Liu, Y. Zhang, Y. Zuo, C. Li, C. Xue, B. Cheng, and Q. Wang, *J. Cryst. Growth* **492**, 29 (2018).
- 4) L. Zhang, H. Hong, Y. Wang, C. Li, G. Lin, S. Chen, W. Huang, and J. Wang, *Chinese Phys. B* **26**, 11 (2017).
- 5) S. Wirths, R. Geiger, N. Von Den Driesch, G. Mussler, T. Stoica, S. Mantl, Z. Ikonik, M. Luysberg, S. Chiuissi, and J. M. Hartmann, *Nat. Photonics* **9**, 88 (2015).
- 6) H. Cong, F. Yang, C. Xue, K. Yu, L. Zhou, N. Wang, B. Cheng, and Q. Wang, *Small* **14**, 1 (2018).
- 7) T. Liu, L. Wang, G. Zhu, X. Hu, Z. Dong, Z. Zhong, Q. Jia, X. Yang, and Z. Jiang, *Semicond. Sci. Technol.* **33**, 12 (2018).
- 8) A. A. Tonkikh, N. D. Zakharov, A. A. Suvorova, C. Eisenschmidt, J. Schilling, and P. Werner, *Cryst. Growth Des.* **14**, 1617 (2014).
- 9) R. Al-Saigh, M. Baira, B. Salem, and B. Ilahi, *Nanoscale Res. Lett.* **13**, 1 (2018).
- 10) R. J. A. Esteves, M. Q. Ho, and I. U. Arachchige, *Chem. Mater.* **27**, 1559 (2015).
- 11) M. S. Seifner, F. Biegger, A. Lugstein, J. Bernardi, and S. Barth, *Chem. Mater.* **27**, 6125 (2015).
- 12) J. Doherty, S. Biswas, D. Saladukha, Q. Ramasse, T. S. Bhattacharya, A. Singha, T. J. Ochalski, and J. D. Holmes, *J. Mater. Chem. C* **6**, 8738 (2018).
- 13) W. Du, S. A. Ghetmiri, J. Margetis, S. Al Kabi, Y. Zhou, J. Liu, G. Sun, R. A. Soref, J. Tolle, and B. Li, *J. Appl. Phys.* **122**, 12 (2017).
- 14) P. C. Grant, J. Margetis, W. Du, Y. Zhou, W. Dou, G. Abernathy, A. Kuchuk, B. Li, J. Tolle, and J. Liu, *Nanotechnology* **29**, 46 (2018).
- 15) D. Carolan, *Prog. Mater. Sci.* **90**, 128 (2017).
- 16) A. Karatutlu, M. Song, A. P. Wheeler, O. Ersoy, W. R. Little, Y. Zhang, P. Puech, F. S. Boi, Z. Luklinska, and A. V. Sapelkin, *RSC Adv.* **5**, 20566 (2015).
- 17) S. A. Hafiz, R. J. A. Esteves, D. O. Demchenko, I. U. Arachchige, and Ü. Özgür, *J. Phys. Chem. Lett.* **7**, 3295 (2016).
- 18) K. Ramasamy, P. G. Kotula, A. F. Fidler, M. T. Brumbach, J. M. Pietryga, and S. A. Ivanov, *Chem. Mater.* **27**, 4640 (2015).
- 19) Y. J. Cho, C. H. Kim, H. S. Im, Y. Myung, H. S. Kim, S. H. Back, Y. R. Lim, C. S. Jung, D. M. Jang, and J. Park, *Phys. Chem. Chem. Phys.* **15**, 116915 (2013).
- 20) H. Lin, R. Chen, Y. Huo, T. I. Kamins, and J. S. Harris, *Appl. Phys. Lett.* **98**, 1 (2011).
- 21) M. Kim, W. Fan, J. H. Seo, N. Cho, S. C. Liu, D. Geng, Y. Liu, S. Gong, X. Wang, and W. Zhou, *Appl. Phys. Express* **8**, 061301 (2015).
- 22) L. Zhang, Y. Wang, N. Chen, G. Lin, C. Li, W. Huang, S. Chen, J. Xu, and J. Wang, *J. Non-Cryst. Solids* **448**, 74 (2016).
- 23) M. Uwaha, in *Handbook of Crystal Growth*, ed. T. Nishinaga (Elsevier, Amsterdam, 2014) 2nd ed., Vol. 1A, p. 360.
- 24) I. Riihimäki, A. Virtanen, S. Rinta-Anttila, P. Pusa, and J. Räisänen, *Appl. Phys. Lett.* **91**, 1 (2007).
- 25) G. Vogel, G. Hettich, and H. Mehrer, *J. Phys. C: Solid State Phys.* **16**, 6197 (1983).
- 26) B. Richter, H. Kühlenbeck, H. J. Freund, and P. S. Bagus, *Phys. Rev. Lett.* **93**, 026805 (2004).
- 27) S. Kasap, C. Koughia, J. Singh, H. Ruda, and S. O'Leary, *Springer Handbook of Electronic and Photonic Materials* (Springer, Boston, MA, 2006), p. 47.
- 28) P. Moontragoon, Z. Ikonik, and P. Harrison, *Semicond. Sci. Technol.* **22**, 742 (2007).
- 29) V. R. D'Costa, C. S. Cook, A. G. Birdwell, C. L. Littler, M. Canonico, S. Zollner, J. Kouvetakis, and J. Menéndez, *Phys. Rev. B* **73**, 125207 (2006).
- 30) N. Naruse, Y. Mera, Y. Nakamura, M. Ichikawa, and K. Maeda, *Appl. Phys. Lett.* **94**, 093104 (2009).
- 31) Y. Wang and N. Herron, *J. Phys. Chem.* **95**, 525 (1991).
- 32) D. W. Jenkins and J. D. Dow, *Phys. Rev. B* **36**, 7994 (1987).